



Title	Evolution of long-period stacking order (LPSO) in Mg ₉₇ Zn ₁ Gd ₂ cast alloys viewed by HAADF-STEM multi-scale electron tomography
Author(s)	Sato, Kazuhisa; Tashiro, Shunya; Matsunaga, Shuhei et al.
Citation	Philosophical Magazine. 2018, 98(21), p. 1945-1960
Version Type	AM
URL	https://hdl.handle.net/11094/97375
rights	© 2018 Informa UK Limited, trading as Taylor & Francis Group.
Note	

The University of Osaka Institutional Knowledge Archive : OUKA

<https://ir.library.osaka-u.ac.jp/>

The University of Osaka

Evolution of long-period stacking order (LPSO) in Mg₉₇Zn₁Gd₂ cast alloys viewed by HAADF-STEM multi scale electron tomography

Kazuhisa Sato^{ab*}, Shunya Tashiro^c, Shuhei Matsunaga^c, Yohei Yamaguchi^c, Takanori Kiguchi^a and Toyohiko J. Konno^a

^aInstitute for Materials Research, Tohoku University, 2-1-1 Katahira, Aoba-ku, Sendai 980-8577, Japan,

^bPresent Address: Research Center for Ultra-High Voltage Electron Microscopy, Osaka University, 7-1 Mihogaoka, Ibaraki 567-0047, Japan,

^cDepartment of Materials Science, Tohoku University, 6-6 Aramaki, Aoba-ku, Sendai 980-8579, Japan

*Corresponding Author: Tel: +81 6-6879-7941; Fax: +81 6-6879-7942; E-mail: sato@uhvem.osaka-u.ac.jp

Keywords

Long-period stacking order (LPSO); magnesium alloys; electron tomography; scanning transmission electron microscopy (STEM); lateral morphology

Abstract

We have studied three-dimensional (3D) structures and growth processes of 14H-type long-period stacking order (LPSO) formed in $\text{Mg}_{97}\text{Zn}_1\text{Gd}_2$ cast alloys by single tilt-axis electron tomography (ET) using high-angle annular dark-field scanning transmission electron microscopy. Evolution of the solute-enriched stacking faults (SFs) and the 14H LPSO by aging were visualized in 3D with a high spatial resolution in multi scale fields of views from a few nanometers to $\sim 10\ \mu\text{m}$. Lateral growth of the solute-enriched SFs and the LPSO in the $(0001)_{\text{Mg}}$ plane is notable compared to the out-of-plane growth in the $[0001]_{\text{Mg}}$ direction. The 14H LPSO grows at the cost of decomposition of the $(\text{Mg}, \text{Zn})_3\text{Gd}$ -type precipitates, and accompany a change of in-plane edge angles from 30° to 60° . We have updated the Time-Temperature-Transformation diagram for precipitation in $\text{Mg}_{97}\text{Zn}_1\text{Gd}_2$ alloys: starting temperatures of both solute-enriched SFs and LPSO formation shifted to a shorter time side than those in the previous diagram.

1. Introduction

Ternary Mg alloys containing Zn together with rare earth (RE) elements have been attracting much interest as next generation lightweight structural materials due to their superior properties, such as low density, high specific strength, damping capacity, and recycling efficiency. The strength of the materials can be attributed to the characteristic long-period stacking order, i.e., synchronized structural and compositional modulations of the stacking order (synchronized LPSO, hereafter denoted by LPSO) [1].

The Mg-Zn-RE alloys can be classified into two categories from the viewpoints of formation processes of the LPSO [2]. Namely, the alloys that can give rise to structures with the LPSO (hereafter denoted by LPSO structures) in the as-cast state are termed as type I, of which Mg-Zn-Y alloy is representative. In their category, 18R-type LPSO exists along grain boundaries and as particles inside the α -Mg matrix having hexagonal closed packed (hcp) structure. They transform to 14H-type LPSO by heat treatments. On the other hand, those where LPSO does not form in as-cast state are so called type II alloys. For example, the Mg-Zn-Gd system belongs to this category [3]. In this alloy system, no LPSO exists in the as-cast state and the 14H-type LPSO is formed by aging at temperatures higher than 623 K. Therefore, the type II alloy is suitable for investigating formation processes of the LPSO as a function of annealing temperature and time. Yamasaki et al. reported the Time-Temperature-Transformation (TTT) diagram for precipitation in $\text{Mg}_{97}\text{Zn}_1\text{Gd}_2$ alloys revealed by TEM and electron diffraction [3].

Recent structural characterization of the LPSO have relied on high-angle annular dark-field scanning transmission electron microscopy (HAADF-STEM) with an improved resolution and chemical sensitivity known as atomic number contrast (Z-contrast). The latest imaging

techniques enable atomic scale characterization of structural and chemical irregularities in the LPSO [4-6]. However, the images obtained by this technique are projections of three-dimensional (3D) objects. To better understand the formation mechanism of the LPSO, visualization of 3D structures is greatly needed. In this respect, electron tomography (ET) has paved a new way: the technique can retrieve 3D structures from two-dimensional (2D) projected images and nowadays it is used in a wide field of materials science [7, 8]. Currently, 3D-ET is an only available technique that can reveal microstructures of bulk structural alloys with a high spatial resolution (>1 nm) in multi scale fields of views (a few nanometer to ~ 10 μm) [9-13].

To visualize 3D microstructures, however, diffraction contrasts should be avoided, which disturb the linearity between image intensity and thickness of the object [14]. Incoherent imaging via a HAADF detector in STEM is a current routine for acquiring tilt-series images of crystalline specimens, which enables us to replicate mass thickness contrasts from non-crystalline materials. To characterize fine details of precipitation behaviors in a Mg-Zn-Gd alloy, combination of 3D-ET and Z-contrast STEM is, therefore, suitable. Our preliminary studies on this topic demonstrated the feasibility of the technique; plate-shaped precipitates with the 14H LPSO enriched in heavy Zn and Gd were clearly detected in the α -Mg matrix [15, 16].

In this paper, we report on the 3D-structural evolution of LPSO formed in $\text{Mg}_{97}\text{Zn}_1\text{Gd}_2$ alloys in intermediate stages of their formation by means of single tilt-axis ET using HAADF-STEM. We show results obtained for the alloys aged at 773 K as a function of time and compared them with those obtained at lower aging temperatures. Formation and growth mechanism of the LPSO, especially lateral morphology, are discussed based on 3D-ET taking

into account recent findings on structural properties.

2. Experimental Procedure

Ingots of the $\text{Mg}_{97}\text{Zn}_1\text{Gd}_2$ (at%) cast alloy were prepared by high-frequency induction melting in an Ar atmosphere. The alloys were annealed at 593, 723, 753, and 773 K in an Ar atmosphere for intervals of 60, 3×10^2 , 9×10^2 and 1.8×10^4 s, and then quenched in ice water. Here, the aging temperatures were selected based on the TTT diagram reported previously [3]. Vickers hardness was measured using a Micro Hardness Tester (Shimadzu HMV-G20) with a load of 0.5 kg and a dwell time of 10 s. To prepare samples for 3D-ET, disk-shaped specimens 3 mm ϕ in diameter were mechanically thinned followed by low-energy Ar ion milling (Gatan PIPS model691).

Microstructures of the alloy were observed using an FEI TITAN³ 60-300 STEM operating at 300 kV. Tilt-series of HAADF-STEM images were obtained sequentially from 0° to -70° and then 0° to +70° with the angular increment of 2° using a single tilt-axis specimen holder (Fischione model 2020). The EXPLORE 3D software (FEI Co. Ltd) was used for datasets acquisition taking the dynamic focus into consideration. We set the electron probe convergence semi-angle to be 10 mrad in order to ensure enough depth of focus for STEM imaging at high-tilt angles [17, 18]. Collection semi-angles on the HAADF-detector were set to 50-200 mrad. Alignment of the tilt-axis of the obtained dataset and subsequent 3D reconstruction were performed via INSPECT 3D software package (FEI Co. Ltd) and COMPOSER software package (System In Frontier, Inc.). We employed weighted back-projection (WBP) method as well as simultaneous iterative reconstruction technique (SIRT) for 3D reconstruction. We compared the reconstructed results and the original HAADF-STEM image, and selected the

optimal reconstruction result in respect of shape and size of the reconstructed precipitates. It should be noted that when strong contrast regions exist together with fine weak contrast objects in the area of interest, reconstruction becomes difficult; in such a case, empirically WBP results in better reconstruction than SIRT [19]. The reconstructed 3D volumes were then visualized using AMIRA 4.1 software (Visage Imaging) or VISUALIZER-KAI software (System In Frontier, Inc.).

3. Results and Discussion

3.1 Formation and growth of LPSO at 773 K

Microstructure changes were monitored by electron diffraction and HAADF-STEM as a function of aging time at 773 K. As-cast alloy contained no solute-enriched stacking faults (SFs) or LPSO other than large precipitates of (Mg, Zn)₃Gd-type secondary phase dispersed in the α -Mg matrix as reported in the literature [3]. Formation of the solute-enriched SFs was detected by electron diffraction as an emergence of weak streaks between fundamental reflections in the $[0001]^*_{\text{Mg}}$ direction after aging for 60 s.

Figure 1(a) shows a HAADF-STEM image of a specimen after aging for 60 s at 773 K. The inset selected area electron diffraction (SAED) pattern was obtained from the α -Mg matrix including the solute-enriched SFs with beam incidence parallel to $[\bar{1}2\bar{1}0]_{\text{Mg}}$. Large precipitates lying across the field of view are the (Mg, Zn)₃Gd phase, which exists in as-cast alloys [3, 19]. Fine bright straight lines are seen almost perpendicular to the precipitate; these thin bands less than 10 nm in thickness can be classified as a set of a few numbers of the solute-enriched SFs, to which solute elements are segregating [3, 6]. Correspondingly, electron diffraction shows

weak streaks in the $[0001]^*_{\text{Mg}}$ direction. Such a dense distribution of the solute-enriched SFs are always observed in adjacent to $(\text{Mg}, \text{Zn})_3\text{Gd}$ precipitates but not in the matrix. There is a depletion zone in between large two precipitates, suggesting that the solute-enriched SFs would be formed beside the precipitates.

Figure 1(b) shows a reconstructed 3D image processed by WBP around the $(\text{Mg}, \text{Zn})_3\text{Gd}$ precipitate after aging for 60 s at 773 K. Solute-enriched SFs are generated with high density on the left of the precipitate, but is hardly on the right. To clearly display fine details of the 3D structure, we used color gradation to visualize 3D reconstructed volume. Thus 3D-ET revealed spatial distribution and morphology of fine SFs with a few to a few tens of nanometers of stacked thickness.

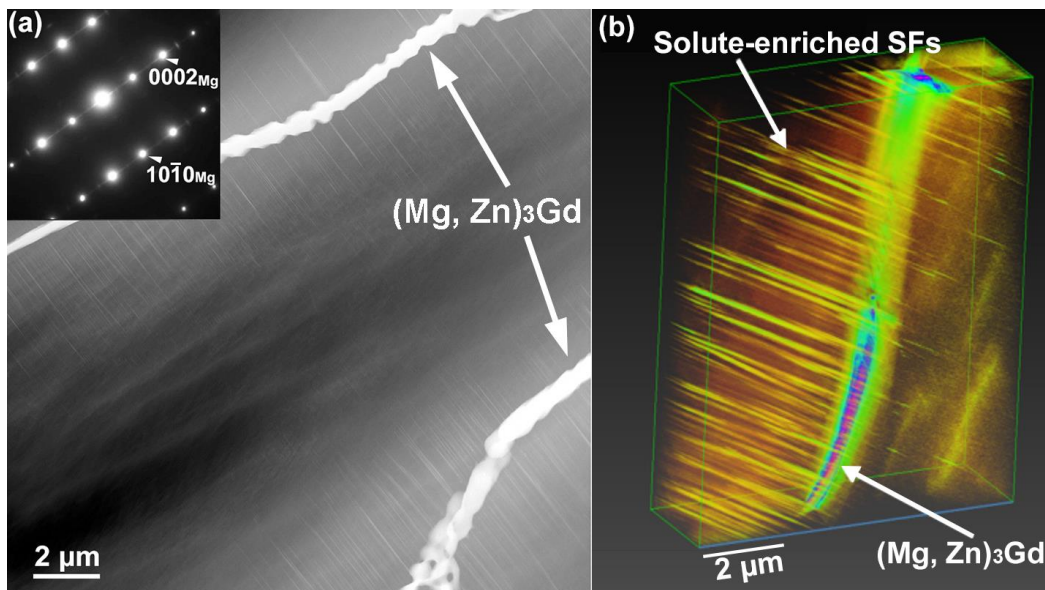


Figure 1. (a) HAADF-STEM image and SAED pattern of a specimen after aging for 60 s at 773 K. Electron diffraction shows weak streaks in the $[0001]^*_{\text{Mg}}$ direction. (b) A snapshot of reconstructed 3D volume processed by WBP around the $(\text{Mg}, \text{Zn})_3\text{Gd}$ -type precipitate. The reconstructed volume is $3.8 \mu\text{m} \times 4.1 \mu\text{m} \times 1.1 \mu\text{m}$ with the pixel size of 8.6 nm.

Figure 2(a) shows another example of reconstructed 3D image processed by WBP for a specimen after aging at 773 K for 60 s. Solute-enriched SFs are densely formed in adjacent to a large $(\text{Mg, Zn})_3\text{Gd}$ precipitate. Figure 2(b) shows a magnified image near the edge of the solute-enriched SFs close to the precipitate. Edge of the SF has a triangular shape as indicated by the circle. Typical examples of lateral morphology of SFs are shown in Fig. 2(c). The edge angles of $\sim 60^\circ$ are seen. At this stage, the lateral length of the SFs in the $[\bar{1}0\bar{1}0]_{\text{Mg}}$ direction is in the range of 500 nm to 2.5 μm , while their stacked layer thickness in the $[0001]_{\text{Mg}}$ direction is less than 10 nm.

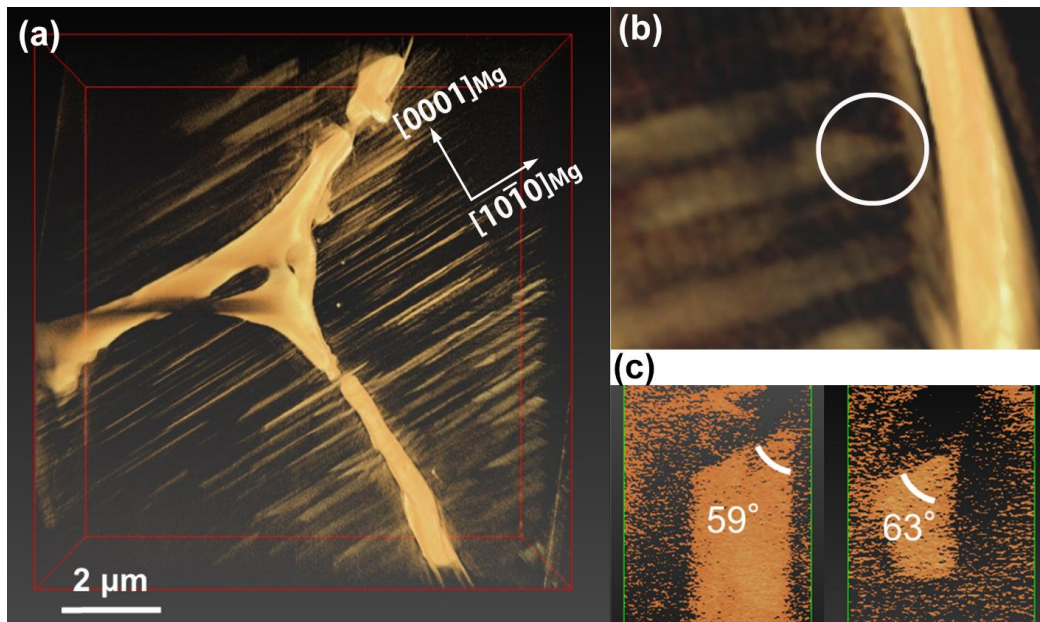


Figure 2 (a) A snapshot of reconstructed 3D image processed by WBP for a specimen after aging at 773 K for 60 s. The reconstructed volume is $10.8 \mu\text{m} \times 10.8 \mu\text{m} \times 4.1 \mu\text{m}$ with the pixel size of 6.1 nm. (b) A magnified image near the edge of the solute-enriched SFs close to the precipitate. (c) Typical examples of lateral morphology of SFs.

Figures 3 (a-d) show part of SAED patterns for specimens after aging for 3×10^2 , 6×10^2 and 9×10^2 s and 1.8×10^4 s at 773 K, respectively. Here, 0001 reflections seen in Figs. 3(a) and 3(d) are double diffraction frequently observed in the case of $[\bar{1}\bar{2}\bar{1}0]_{\text{Mg}}$ incidence. The other two patterns shown in Figs. 3(b) and 3(c) were observed with beam incidence of higher order zone axes exciting 000 l systematic reflections. In Fig.3 (a), intensity modulation, composed of weak six intensity maxima, can be seen in the streak pattern; these faint satellite reflections indicate the onset of the 14H LPSO structure formation. At this stage the LPSO appear in adjacent to a $(\text{Mg}, \text{Zn})_3\text{Gd}$ precipitate as thin plates (hereafter denoted as LPSO plates) with a thickness less than 20 nm in the $[0001]_{\text{Mg}}$ direction, which is approximately 5 structural units with the periodicity of 3.64 nm. After aging for 6×10^2 s, weak intensity maxima emerge in the streak pattern shown in Fig. 3(b). After aging for 9×10^2 s, splitting of six satellite reflections became clear as shown in Fig. 3(c). After aging for 1.8×10^4 s, satellite reflections with considerable intensity are clearly seen in the $[0001]^*_{\text{Mg}}$ direction as shown in Fig. 3(d), indicating the development of LPSO.

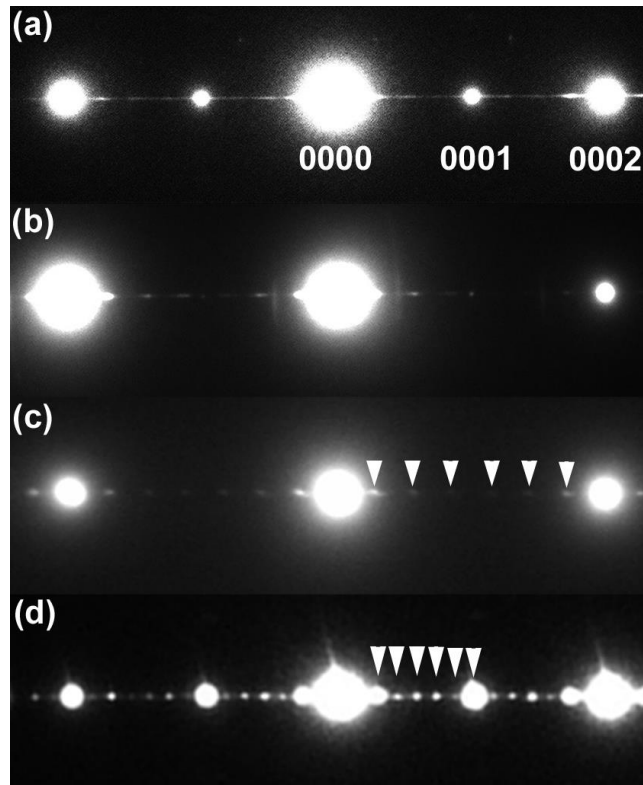


Figure 3 Electron diffraction patterns for specimens after aging at 773 K for 3×10^2 s (a), 6×10^2 s (b), 9×10^2 s (c) and 1.8×10^4 s (d), showing splitting of six satellite reflections by aging.

Figure 4(a) shows a snapshot of reconstructed 3D image processed by WBP for a specimen after aging at 773 K for 9×10^2 s. Lateral morphology near the edge of the solute-enriched SFs is clearly seen in the rotated image shown in Fig. 4(b). The edge angles measured from the reconstructed volume are mostly $\sim 60^\circ$. Lateral length of the solute-enriched SFs in the $[10\bar{1}0]_{\text{Mg}}$ direction distributes between 500 nm and 4 μm , and their stacked layer thickness in the $[0001]_{\text{Mg}}$ direction is 20-30 nm. Particulate precipitates ~ 20 nm in diameter were frequently observed as shown in Figs. 4(a) and 4(b).

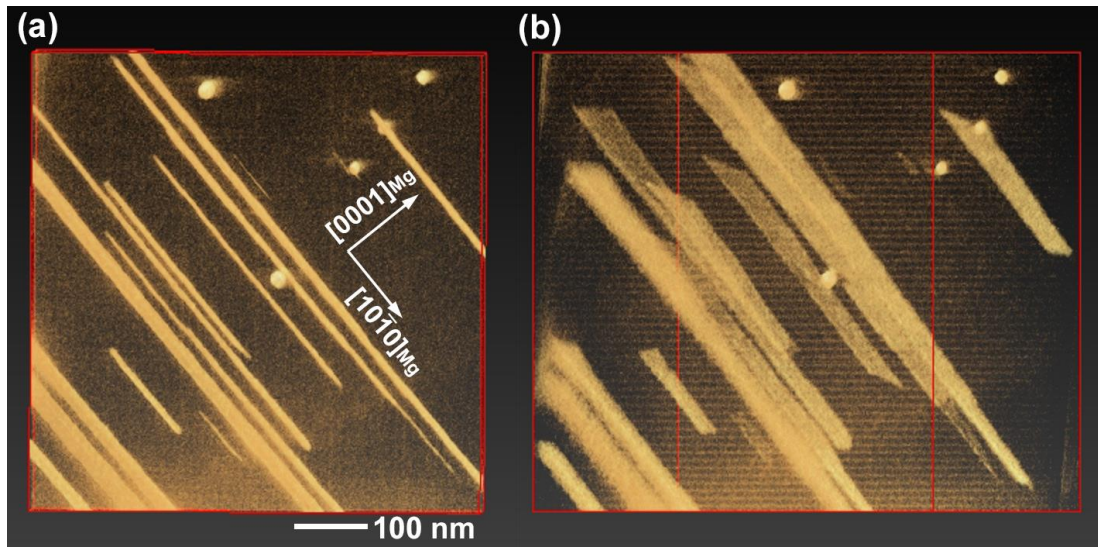


Figure 4 (a) A snapshot of reconstructed 3D image processed by WBP for a specimen after aging at 773 K for 9×10^2 s. The reconstructed volume is $606 \text{ nm} \times 678 \text{ nm} \times 378 \text{ nm}$ with the pixel size of 0.54 nm. (b) An oblique view of the reconstructed volume. Lateral morphology near the edge of the solute-enriched SFs is clearly seen.

Figure 5 shows a representative example of reconstructed 3D volume processed by SIRT for a specimen after aging at 773 K for 1.8×10^4 s. As seen, shapes and distribution of the LPSO plates are reproduced. At this stage, the LPSO grew typically ~ 50 nm thick in the $[0001]_{\text{Mg}}$ direction, and some of them reached as thick as 200 nm. The images viewed in oblique directions reveal existence of an in-plane “dent-shaped” area of an LPSO plate as indicated by arrows. Also note that characteristic triangular shapes can be seen at the edge of some LPSO plates as indicated by circles. These characteristic in-plane shapes have been pointed out in our previous study [15]. Lateral atomic configuration of LPSO has been investigated using scanning tunneling microscopy as well [21, 22], while the 3D-ET can cover a wider field of view.

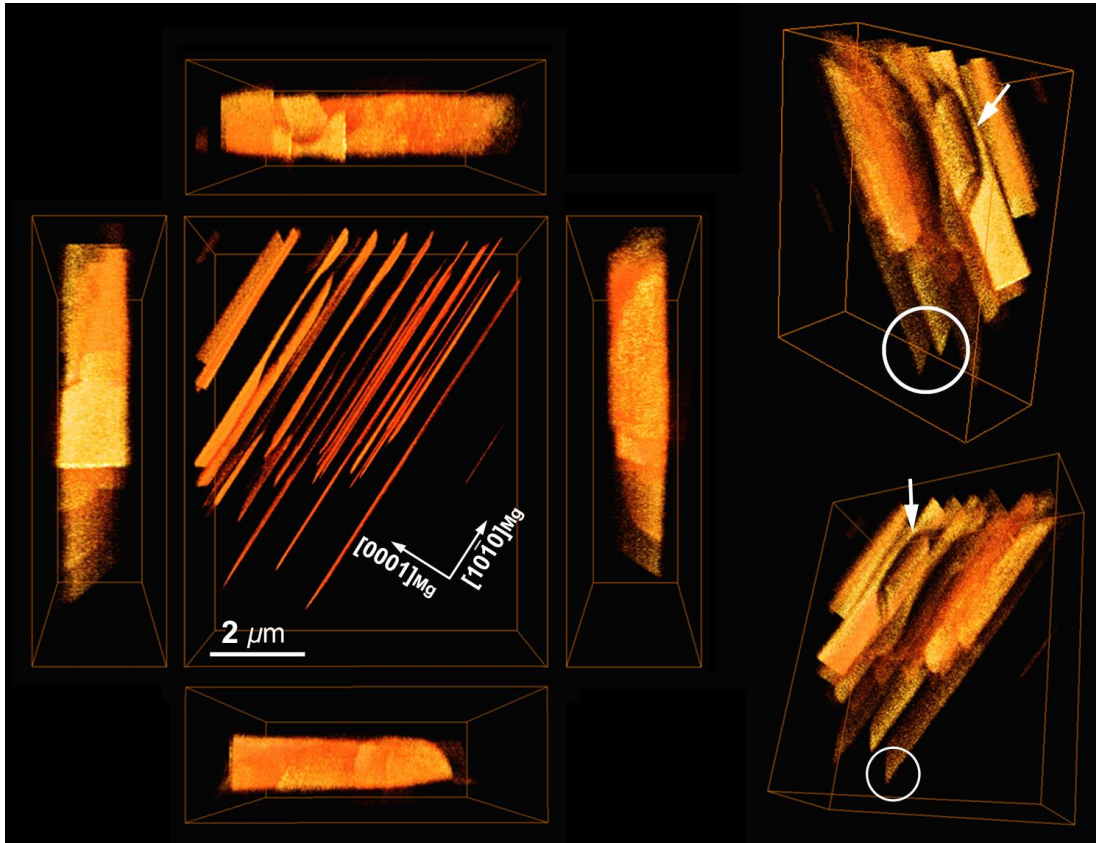


Figure 5 An example of reconstructed 3D images processed by SIRT for a specimen after aging at 773 K for 1.8×10^4 s viewed from several directions. The reconstructed volume is $7.2 \mu\text{m} \times 9.0 \mu\text{m} \times 2.7 \mu\text{m}$ with a pixel size of 12.1 nm. The arrows indicate the in-plane “dent-shaped” area of the LPSO. A characteristic triangular shape can be seen at the edge of an LPSO band as indicated by circles.

Figure 6(a) shows a histogram of in-plane edge angles of the LPSO plates measured from the reconstructed volume. The total counting number was 76. As seen, the edge angles distribute between 30° and 90° , and angles around 60° are dominant. Compared with our preceding study [15], we increased the number of measured angles by twice, but the tendency has not changed. These angles reflect crystallographic features of the 14H LPSO that grow parallel to the (0001) planes of the α -Mg matrix. Figure 6(b) shows crystallographic orientations and schematic

models of lateral morphology of LPSO deduced from 3D reconstructed volumes and electron diffraction patterns. Here, the angle of 60° corresponds to $(11\bar{2}0)_{\text{Mg}}$, while the angles of 30° and 90° correspond to $(01\bar{1}0)_{\text{Mg}}$ and $(10\bar{1}0)_{\text{Mg}}$, respectively. The frequent occurrence of edge angle of 60° implies that $\{11\bar{2}0\}_{\text{Mg}}$ is a preferable plane for lateral growth of LPSO in the α -Mg matrix.

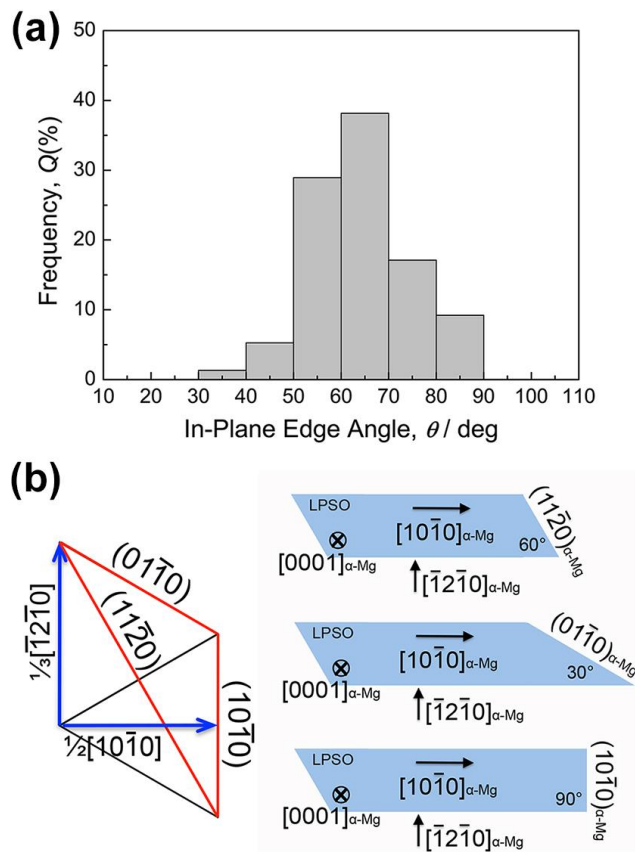


Figure 6 (a) A histogram of in-plane edge angles of 14H LPSO plates obtained from a $\text{Mg}_{97}\text{Zn}_1\text{Gd}_2$ cast alloys after aging at 773 K for 1.8×10^4 s. (b) Schematic models of lateral morphology of LPSO deduced from 3D reconstructed volumes and electron diffraction patterns.

Figure 7 shows a schematic model of growth mechanism of the 14H LPSO at 773 K based on the results of 3D-ET and HAADF-STEM observation. An as-cast alloy contains (Mg,

$(\text{Mg, Zn})_3\text{Gd}$ precipitates dispersed in the $\alpha\text{-Mg}$ matrix. Dissolution of the precipitates and hence enrichment of solute atoms in the $\alpha\text{-Mg}$ matrix proceed by aging at 773 K. Formation of the solute-enriched SFs was noticed after aging for 60 s at 773 K. At this stage, in-plane edge angles for many of the solute-enriched SFs were already reached around 60° , as in the case of grown LPSO. Formation of the thin 14H LPSO plates and shrink of the $(\text{Mg, Zn})_3\text{Gd}$ precipitates were detected after aging for 3×10^2 s at 773 K. After aging at 773 K over 9×10^2 s, 14H LPSO grows in the out-of-plane direction and particulate precipitates remain in adjacent to the LPSO plates.

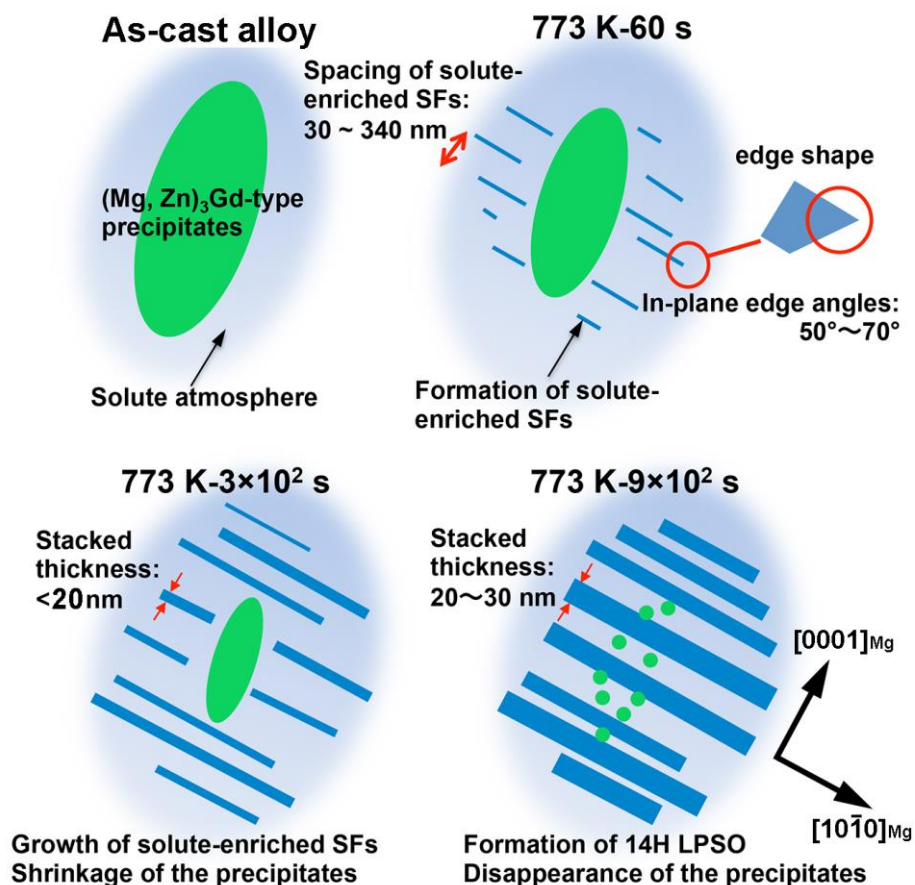


Figure 7 A schematic model of growth mechanism of the 14H LPSO at 773 K based on the results of 3D-ET and elemental analyses. $(\text{Mg, Zn})_3\text{Gd}$ precipitates shrink and the fine 14H LPSO grows.

3.2 Formation and growth of LPSO at 753 K and 723 K

Formation of solute-enriched SFs and their evolution to LPSO at 753 K followed a similar manner to those at 773 K, while it took a longer aging time. The growth sequence at 753 K is summarized as follows: weak streaks were detected after aging for 3×10^2 s, and the splitting of the streaks into six satellite spots was recognized after aging for 6×10^2 s. Clear satellite reflections were observed after aging for 9×10^2 s.

Figure 8(a) shows a reconstructed 3D image processed by WBP for a specimen after aging at 753 K for 9×10^2 s. LPSO grows in two different directions from the grain boundary. In the grain marked as A, overlapping of LPSO plates is seen, just like sliding cards. The edge of the LPSO plate shows a triangular shape as indicated by a circle. Histograms of the stacked layer thickness of the LPSO plates in the $[0001]_{\text{Mg}}$ direction are shown in Fig. 8(b). There are two peaks in the histogram for the grain A, 15~20 nm and 30~40 nm, with the latter being dominant. In contrast, the grain B shows single peak at around 20~25 nm. Namely, growth of LPSO is more advanced in the grain A than in the B. Figure 8(c) shows a histogram of edge angles of the LPSO plates both for grains A and B. In-plane edge angles are larger for the grain A (40-70°) than for B (10-40°). This observation indicates a correlation between the stacked layer thickness and the edge angle: the edge angle approaches 60° as the LPSO grows. This reasoning may explain the observed edge-angle distribution shown in Fig. 6(a) where the angles around 60° are dominant after the prolonged aging at 773 K for 1.8×10^4 s.

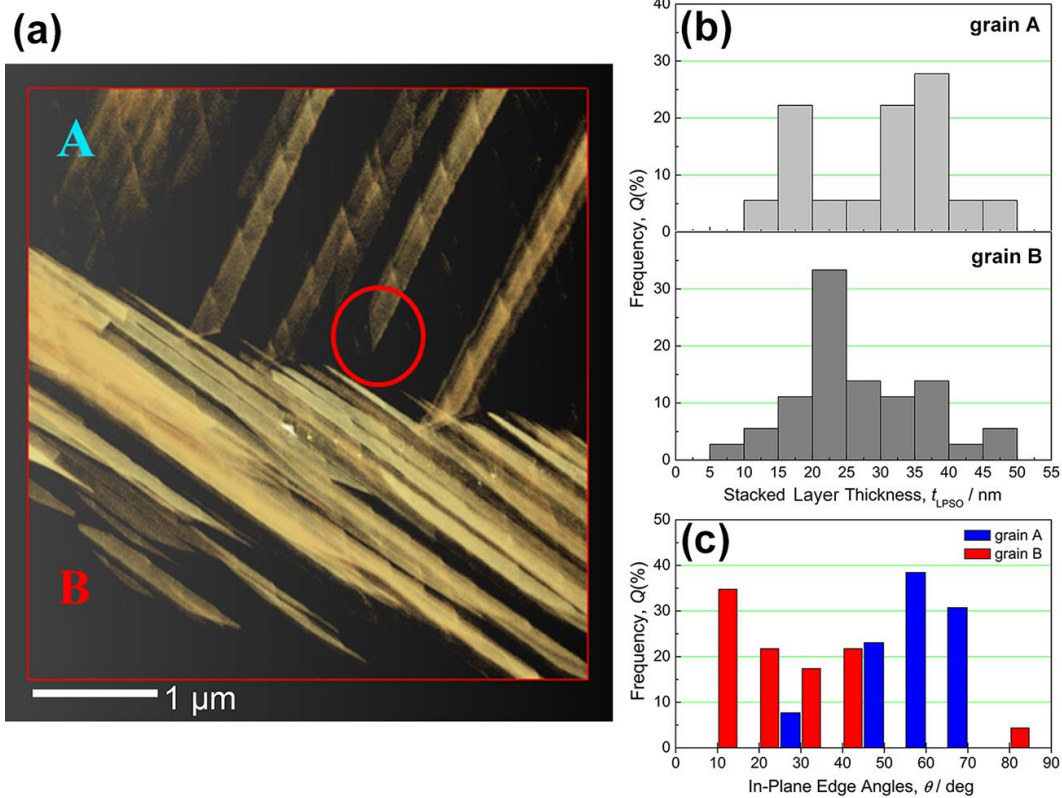


Figure 8 (a) A reconstructed 3D image processed by WBP for a specimen after aging at 753 K for 9×10^2 s. The reconstructed volume is $3.6 \mu\text{m} \times 4.5 \mu\text{m} \times 1.4 \mu\text{m}$ with a pixel size of 6.1 nm. Note the “staggered” contrasts within the LPSO. (b) Histograms of the stacked layer thickness of the LPSO bands in the $[0001]_{Mg}$ direction. (c) A histogram of edge angles of the LPSO plates both for grains A and B.

Similarly, the growth sequence at 723 K is summarized as follows: weak streaks were detected after aging for 9×10^2 s, and the splitting of the streaks into six satellite spots was recognized after aging for 1.8×10^3 s. Clear satellite reflections were observed after aging for 1.8×10^4 s. Figure 9(a) shows a reconstructed 3D image processed by WBP for a specimen after aging at 723 K for 1.8×10^4 s. LPSO grows in two different directions at the grain boundary. Histograms of the stacked layer thickness of the LPSO plates in the $[0001]_{Mg}$ direction are

shown in Fig. 9(b). Both the grains A and B show single peak at around 25~30 nm. Figure 9(c) shows a histogram of in-plane edge angles of the LPSO plates for the grain B. There are two peaks in edge angles: 30-40° and 60-70°. The 723-K-aged specimen has a thinner stacked layer thickness than the 753-K-aged specimen and in-plane edge angles show two peaks near 30° and 60°, indicating that LPSO is not well developed. Since the number of clear in-plane edge of the grain A was few in the reconstructed volume, the analysis of the edge angles was performed only on the grain B.

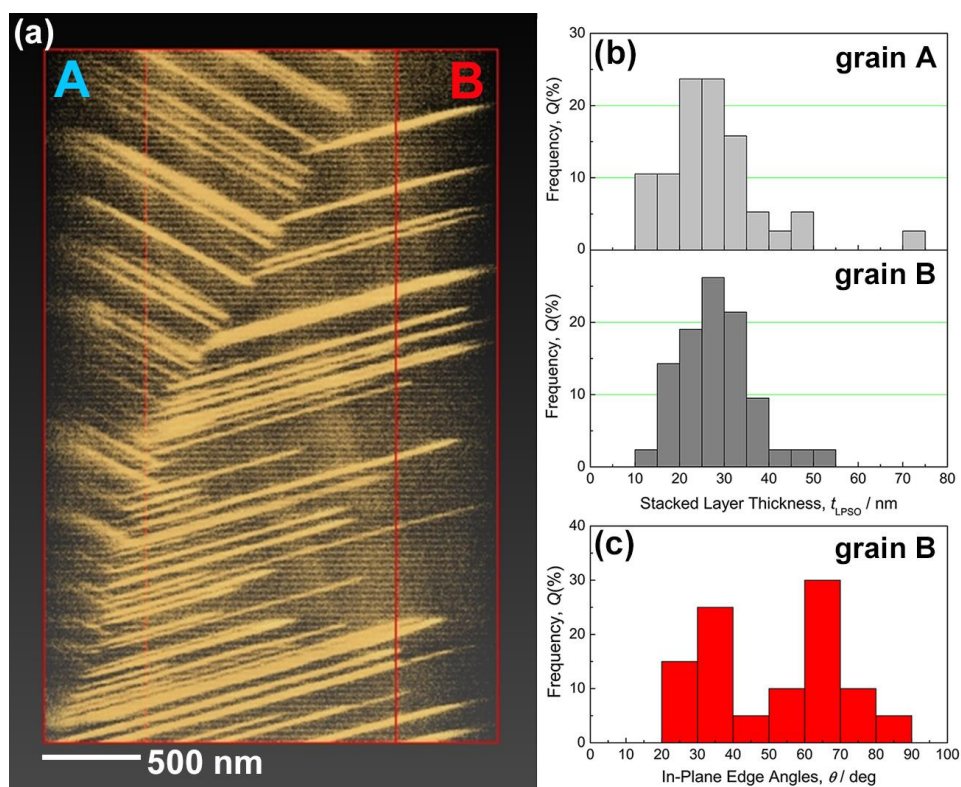


Figure 9 (a) A reconstructed 3D image processed by WBP for a specimen after aging at 723 K for 1.8×10^4 s. The reconstructed volume is $2.7 \mu\text{m} \times 3.5 \mu\text{m} \times 0.7 \mu\text{m}$ with a pixel size of 3.1 nm. (b) Histograms of the stacked layer thickness of the LPSO bands in the $[0001]_{Mg}$ direction. (c) A histogram of edge angles of the LPSO plates for the grain B.

3.4 Changes of mechanical properties by aging and its relation to LPSO formation

Figure 10 shows aging time dependence of the micro Vickers hardness (a) and stacked layer thickness in the $[0001]_{\text{Mg}}$ direction (b) of the specimens aged at 723, 753 and 773 K. Vickers hardness increases from 70 up to 80 H_v by aging over 6×10^2 s, while the increment is at most 14%. As the aging proceeds at 773 K and 753 K, stacked layer thickness rapidly increases between 60 s and 9×10^2 s. At 723 K, longer time was necessary for the growth of LPSO and the increase in stacked layer thickness was observed between 9×10^2 s and 1.8×10^4 s. Thus, the observed age-hardening corresponds to the growth of LPSO, although the effect of LPSO plates distribution on the hardening is small.

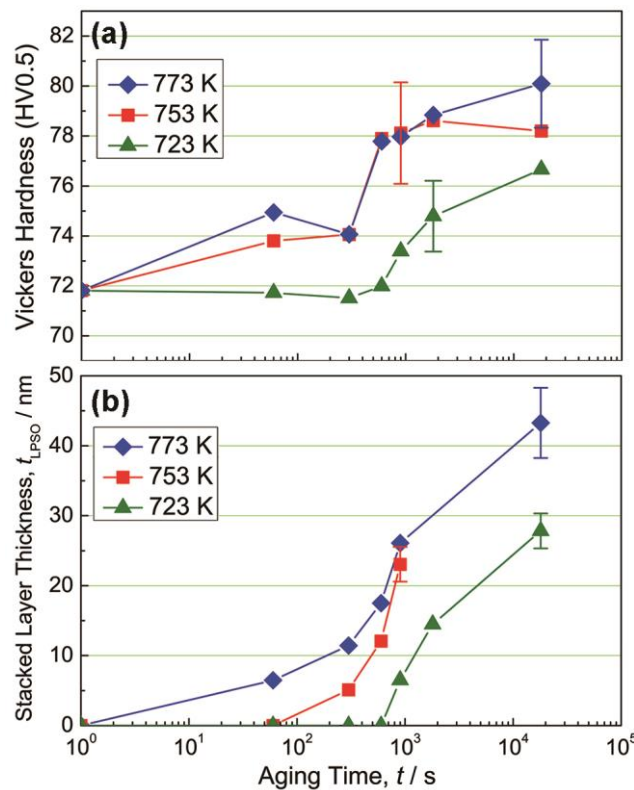


Figure 10 Aging time dependence of the micro Vickers hardness (a) and stacked layer thickness in the $[0001]_{\text{Mg}}$ direction (b) of the specimens aged at 723, 753 and 773 K.

3.5 Growth of solute-enriched SFs at 593 K

The aging temperature of 593 K is close to the lower bound temperature of the LPSO formation on the TTT diagram reported in the literature [3]. Figure 11 shows changes of stacked layer thickness (a) and in-plane edge angles (b) as a function of aging time at 593 K. As seen, stacked layer thickness increases and edge angles change from 30° to 60° as the aging proceeds. This result clearly demonstrated that aging for 1.8×10^4 s at 593 K lead to a formation of solute-enriched SFs and/or fine 14H LPSO with edge angles of around 60°. Thus, it was found that the formation and growth processes are similar to the case aged at higher temperatures. These results suggest stability of the in-plane edge angles of 60° parallel to the $\{11\bar{2}0\}_{\text{Mg}}$.

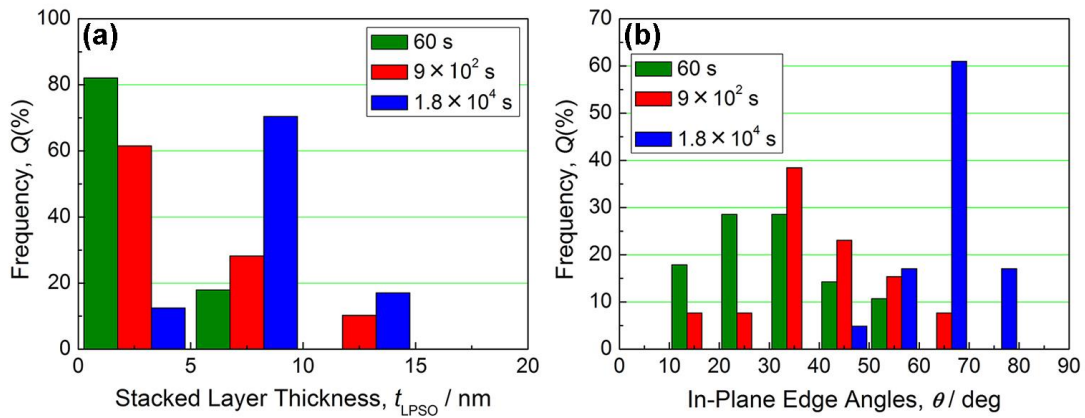


Figure 11 Changes of stacked layer thickness (a) and in-plane edge angles (b) as a function of aging time at 593 K. Edge angles change from 30° to 60° as the aging proceeds.

3.6 Variation of in-plane edge angles of LPSO plates

In-plane edge of each LPSO plate has characteristic triangular shapes with edge angle of around 60° with respect to $\{12\bar{1}0\}_{\text{Mg}}$. In our earlier studies [15, 16], we found that edge angles distribute between 30° and 90°, with the most frequent appearance of ~60°, which corresponds

to a growth front parallel to $\{11\bar{2}0\}_{\text{Mg}}$. The present observations for specimens aged under several conditions revealed that the edge angles change from 30° to 60° as the LPSO grows. Figure 12 shows schematic models explaining the observed change of edge angles. At the initial stage of solute-enriched SFs formation, in-plane close-packed direction is parallel to the $(01\bar{1}0)_{\text{Mg}}$ as shown in Fig.12(a). This results in the edge angle of 30° . As the LPSO grows, in-plane periodic arrangement of $L1_2$ -type atomic clusters is formed [5]. The atomic cluster arrangement changes the in-plane close-packed direction; the close-packed direction of the $2\sqrt{3} \times 2\sqrt{3}$ ordered structure is on a line parallel to the original $(11\bar{2}0)_{\text{Mg}}$ [5]. Thus the edge angles become 60° as shown in Fig. 12(b). This is a simple geometric consideration, but it explains the experimental results well. Okuda et al. revealed the atomic cluster formation prior to the development of LPSO [23].

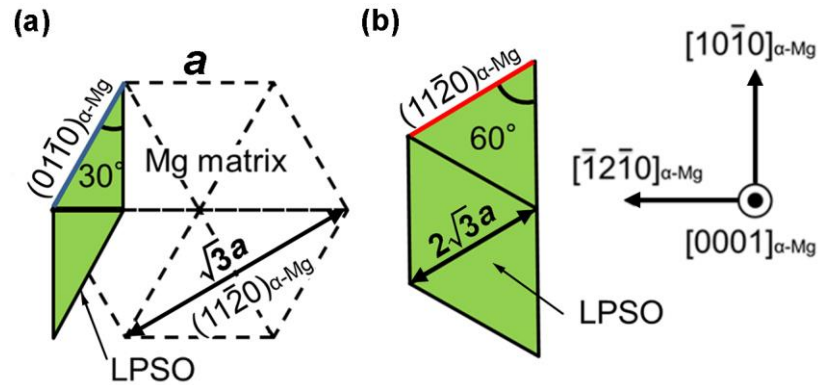


Figure 12 Schematic models explaining the change of edge angles: (a) initial stage of the LPSO formation, (b) after the development of LPSO band with in-plane atomic clusters. In-plane edge angles change from 30° to 60° as the LPSO grows.

3.7 An updated TTT diagram based on 3D-ET

Figure 13 summarized the TTT diagram revised based on our results on 3D-ET using the

HAADF-STEM. Solid circles denote the data points obtained in this study. Diagonal solid lines indicate updated starting temperatures of both solute-enriched SFs and 14H LPSO formation. Dotted lines indicate a part of the TTT diagram for LPSO formation in $Mg_{97}Zn_1Gd_2$ alloys reported in the literature [3]. Starting temperatures of both solute-enriched SFs and 14H LPSO formation shifted to a shorter time side compared to the previously reported TTT diagram. The modification of the TTT diagram would be due to improvement in detection efficiency via chemically sensitive HAADF-STEM with high spatial resolution.

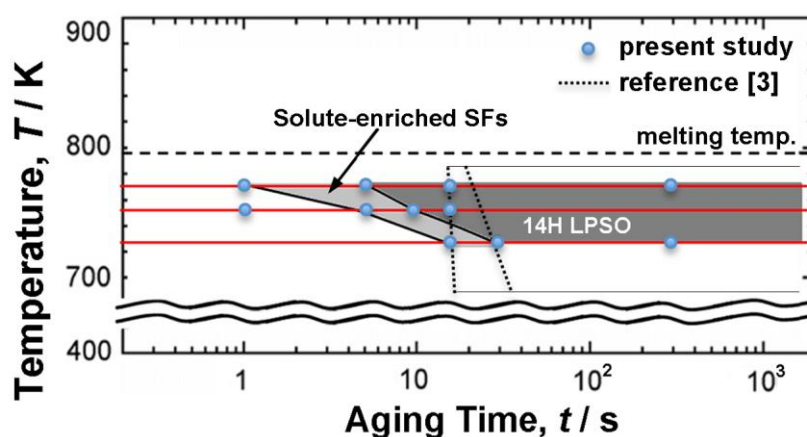


Figure 13 An updated TTT diagram based on the results on 3D-ET using HAADF-STEM. Solid circles denote the data points obtained in this study. Dotted lines indicate a part of the TTT diagram for LPSO formation in $Mg_{97}Zn_1Gd_2$ alloys reported in the literature [3]. Both solute enriched SFs and LPSO formation start temperatures shifted to short time side compared to the previously reported TTT diagram.

4. Conclusion

We have studied 3D structures and growth processes of the 14H LPSO formed in $Mg_{97}Zn_1Gd_2$ cast alloys by HAADF-STEM electron tomography in multi-scale fields of views. The main

results can be summarized as follows.

- (1) The $(\text{Mg}, \text{Zn})_3\text{Gd}$ precipitates act as a source of solute Zn and Gd atoms for the formation and growth of solute-enriched SFs. The 14H LPSO grows at the cost of decomposition of the $(\text{Mg}, \text{Zn})_3\text{Gd}$ precipitates.
- (2) As the solute enriched SFs or the LPSO grows, in-plane edge angles approach to 60° irrespective of the aging conditions. Development of in-plane atomic cluster arrangement changes the in-plane close-packed direction to a line parallel to the original $\{11\bar{2}0\}_{\text{Mg}}$, which is responsible for the observed in-plane edge angles of 60° .
- (3) Lateral growth of the solute enriched SFs and the LPSO is far dominant compared to the out-of-plane growth in the $[0001]_{\text{Mg}}$ direction.
- (4) The TTT diagram for precipitation in $\text{Mg}_{97}\text{Zn}_1\text{Gd}_2$ alloys has been revised: starting temperatures of both solute-enriched SFs and LPSO formation shifted to a shorter time side compared to the previous diagram.

Acknowledgements

The authors wish to thank Prof. Y. Kawamura and Dr. M. Yamasaki in Kumamoto University for providing us Mg-Zn-Gd alloys, and Ms. K. Ito for 3D reconstruction.

Funding

This study was supported by JSPS KAKENHI grant numbers JP26109702 and JP23109006. KS acknowledges financial support from the Japan Science Technology Agency “Development

of systems and technology for advanced measurement and analysis” program and the Tanikawa Fund Promotion of Thermal Technology.

References

- [1] Y. Kawamura, K. Hayashi, A. Inoue, and T. Masumoto, *Rapidly solidified powder metallurgy Mg₉₇Zn₁Y₂ alloys with excellent tensile yield strength above 600 MPa*, Mater. Trans. 42 (2001) 1172-1176.
- [2] Y. Kawamura and M. Yamasaki, *Formation of mechanical properties of Mg₉₇Zn₁RE₂ alloys with long-period stacking ordered structure*, Mater. Trans. 48 (2007), pp.2986-2992.
- [3] M. Yamasaki, M. Sasaki, M. Nishijima, K. Hiraga, and Y. Kawamura, *Formation of 14H long period stacking ordered structure and profuse stacking faults in Mg-Zn-Gd alloys during isothermal aging at high temperature*, Acta Mater. 55 (2007), pp.6798-6805.
- [4] E. Abe, A. Ono, T. Itoi, M. Yamasaki, and Y. Kawamura, *Polytypes of long-period stacking structures synchronized with chemical order in a dilute Mg-Zn-Y alloy*, Philos. Mag. Lett. 91 (2011), pp.690-696.
- [5] H. Yokobayashi, K. Kishida, H. Inui, M. Yamasaki, and Y. Kawamura, *Enrichment of Gd and Al atoms in the quadruple close packed planes and their in-plane long-range ordering in the long period stacking-ordered phase in the Mg-Al-Gd system*, Acta Mater. 59 (2011), pp.7287-7299.
- [6] T. Kiguchi, Y. Ninomiya, K. Shimmi, K. Sato, and T. J. Konno, *Structural and compositional modulation in transformation of LPSO structure in Mg₉₇Zn₁Y₂ cast alloys*, Mater. Trans. 54 (2013), pp.668-674.
- [7] P. A. Midgley and M. Weyland, *3D electron microscopy in the physical sciences: the development of Z-contrast and EFTEM tomography*, Ultramicrosc. 96 (2003), pp.413-431.
- [8] H. Friedrich, M. R. McCartney, and P. R. Buseck, *Comparison of intensity distributions in*

- tomograms from BF TEM, ADF STEM, HAADF STEM, and calculated tilt series*, Ultramicrosc. 106 (2005), pp.18-27.
- [9] J. S. Barnard, J. Sharp, J. R. Tong and P. A. Midgley, *Three-dimensional analysis of dislocation networks in GaN using weak-beam dark-field electron tomography*, Philos. Mag. 86 (2006), pp.4901-4922.
- [10] A. Takaoka, T. Hasegawa, K. Yoshida and H. Mori, *Microscopic tomography with ultra-HVEM and applications*, Ultramicrosc. 108 (2008), pp.230-238.
- [11] S. Benlekber, T. Epicier, M. Bausach, M. Aouine and G. Berhault, *STEM HAADF electron tomography of palladium nanoparticles with complex shape*, Philos. Mag. Lett. 89 (2009), pp.145-153.
- [12] S. Hata, H. Miyazaki, S. Miyazaki, M. Mitsuhashi, M. Tanaka, K. Kaneko, K. Higashida, K. Ikeda, H. Nakashima, S. Matsumura, J. S. Barnard, J. H. Sharp and P. M. Midgley, *High-angle triple-axis specimen holder for three-dimensional diffraction contrast imaging in transmission electron microscopy*, Ultramicrosc. 111 (2011), pp.1168-1175.
- [13] H. Jinnai, T. Tsuchiya, S. Motoki, T. Kaneko, T. Higuchi and A. Takahara, *Transmission electron microtomography in soft materials*, Microsc. 62 (2013), pp.243-258.
- [14] J. Yamasaki, M. Mutoh, S. Ohta, S. Yuasa, S. Arai, K. Sasaki and N. Tanaka, *Analysis of nonlinear intensity attenuation in bright-field TEM images for correct 3D reconstruction of the density in micron-sized materials*, Microscopy 63 (2014), pp.345-355.
- [15] K. Sato, S. Matsunaga, S. Tashiro, Y. Yamaguchi, T. Kiguchi, and T. J. Konno, *Three-Dimensional Shapes and Distribution of Long-Period Stacking Ordered Structures in Mg₉₇Zn₁Gd₂ Cast Alloys Characterized by Electron Tomography*, Mater. Trans. 56 (2015),

pp.928-932.

- [16] K. Sato, S. Tashiro, Y. Yamaguchi, T. Kiguchi, T. J. Konno, T. Yamamoto, K. Yasuda, and S. Matsumura, *Three-Dimensional Imaging of a Long-Period Stacking Ordered Phase in $Mg_{97}Zn_1Gd_2$ Using High-Voltage Electron Microscopy*, Mater. Trans. 57 (2016), pp.918-922.
- [17] P. D. Nellist, *The Principles of STEM Imaging*, in *Scanning Transmission Electron Microscopy*, S. J. Pennycook and P. D. Nellist ed. (Springer, NY, 2011), pp.91-115.
- [18] T. Kiguchi, Y. Yamaguchi, S. Tashiro, K. Sato, and T. J. Konno, *Effect of focal depth of HAADF-STEM imaging on the solute enriched layers in Mg alloys*, Mater. Trans. 56, 1633 (2015).
- [19] Y. Jono, M. Yamasaki, and Y. Kawamura, *Effect of LPSO phase-stimulated texture evolution on creep resistance of extruded Mg-Zn-Gd alloys*, Mater. Trans. 54 (2013), pp.703-712.
- [20] K. Sato, S. Semboshi and T. J. Konno, *Three-dimensional imaging of dislocations in a Ti-35mass%Nb alloy by electron tomography*, Materials 8 (2015), pp.1924-1933.
- [21] S. Kurokawa, A. Yamaguchi and A. Sakai, *An attempt to image chemical ordering in close-packed layer of Mg-Zn-Y 18R long-period stacking-ordered structure by scanning tunneling microscopy*, Mater. Trans. 54 (2013), pp.1073-1076.
- [22] H. Kimizuka, S. Kurokawa, A. Yamaguchi, A. Sakai and S. Ogata, *Two-dimensional ordering of solute nanoclusters at a close-packed stacking fault: modeling and experimental analysis*, Scientific Rep. 4 (2014), pp.7318 1-9.
- [23] H. Okuda, M. Yamasaki, Y. Kawamura, M. Tabuchi, and H. Kimizuka, *Nanoclusters first:*

a hierarchical phase transformation in a novel Mg alloy, Scientific Rep. 5 (2015),
pp.14186 1-6.